

# Investigation of mechanical and corrosion properties of an Al–Zn–Mg–Cu alloy under various ageing conditions and interface analysis of $\eta'$ precipitate

Wenchao Yang<sup>a,c,d,\*</sup>, Shouxun Ji<sup>c</sup>, Qian Zhang<sup>b</sup>, Mingpu Wang<sup>d</sup>

<sup>a</sup> State Key Laboratory of Solidification Processing, Northwestern Polytechnical University, Xi'an 710072, China

<sup>b</sup> Gränges Aluminium Co., Ltd., Shanghai 201807, China

<sup>c</sup> Brunel Centre for Advanced Solidification Technology (BCAST), Brunel University London, Uxbridge UB8 3PH, UK

<sup>d</sup> School of Materials Science and Engineering, Central South University, Hunan, Changsha 410083, China

## A B S T R A C T

The mechanical and corrosion properties under various ageing treatment conditions were investigated in an Al–6.0Zn–2.3Mg–1.8Cu–0.1Zr (wt.%) alloy. The results showed that the retrogression and re-ageing (RRA) were capable of providing higher strength and improved corrosion resistance in comparison with the conventional T6 and T74 ageing. The optimised ageing process had been found to be 120 °C/24 h + 180 °C/60 min + 120 °C/24 h for the experimental alloy. The results obtained from the high resolution transmission electron microscopy (HRTEM) interface analysis revealed that a semi-coherent stress field between the  $\eta'$  precipitate and the Al matrix was critical in controlling the strength of the Al–Zn–Mg–Cu alloy heat-treated under different conditions. Furthermore, Transition Matrix calculation showed that the  $\eta'$  phases had only two zone axes:  $[\bar{1}\bar{2}\bar{3}]_{\eta'}$  and  $[10\bar{8}\bar{2}3]_{\eta'}$ , which were parallel to the  $[112]_{Al}$  zone axis, when being precipitated from the Al matrix. Therefore, the orientation relationships between the  $\eta'$  precipitates and the Al matrix under the  $[112]_{Al}$  zone axis could be described as:  $[\bar{1}\bar{2}\bar{3}]_{\eta'}/[112]_{Al}; (1\bar{2}12)_{\eta'}/(1\bar{1})_{Al}$  and  $[10\bar{8}\bar{2}3]_{\eta'}/[112]_{Al}; (1\bar{2}12)_{\eta'}/(1\bar{1})_{Al}$ . Consequently, a new diffraction pattern model from  $\eta'$  precipitates in two variants under the  $[112]_{Al}$  zone axis had been established, which was in a good agreement with the experimental data.

## 1. Introduction

The application of aluminium alloys in motor vehicles and other types of transportation equipment is becoming one of the most important ways to reduce structural weight, which can effectively lower fuel consumption and improve vehicle performance [1,2]. The combination of the relatively low mass of aluminium alloys with the improved strength, flexibility and other performance is essential to achieve light-weighting in transport structure [3,4]. Therefore, the aluminium alloys and the associated processing techniques need to be developed to maximise the performance while maintaining minimum costs.

The strengthening of the heat-treatable wrought Al–Zn–Mg–Cu aluminium alloy is predominately determined by the type and size of precipitates [5–7]. The precipitation sequence is usually described as: supersaturated solid solution  $\rightarrow$  GP zones  $\rightarrow$   $\eta'$  phase  $\rightarrow$   $\eta$  phase. The GP zones are generally formed during a natural ageing or in the early stage of an artificial ageing, which serve as nucleation sites for the formation of metastable  $\eta'$  phase. It has been found that the metastable

$\eta'$  phase, rather than the stable  $\eta$  phase ( $MgZn_2$ ), is solely responsible for the peak hardening of Al–Zn–Mg–Cu alloys [8].

However, in the wrought Al–Zn–Mg–Cu alloys, the corrosion resistance is generally not sufficiently good to satisfy the industrial requirements. Moreover, the high strength and the satisfied corrosion resistance are difficult to achieve in the same time because the alloys are always sensitive to local corrosions including the intergranular corrosion, exfoliation corrosion and stress corrosion cracking (SCC) [9,10]. However, both the strength and the corrosion resistance of the alloy are equally important in application and these are closely associated with the microstructural characteristics, in particular the size and distribution of precipitates and precipitate-free zone (PFZ) at the grain boundaries [11,12]. Therefore, in order to obtain a combination of good corrosion resistance and improved strength, the microstructural control of the precipitates in the primary aluminium grains and at grain boundaries becomes essential for Al–Zn–Mg–Cu alloys. It is known that the heat treatment is an effective approach to modify the microstructure of wrought aluminium alloys. However, the commonly used T6 treatment can improve the strength, but worsen the local corrosion resistance [13]. On the other hand, several over-aged treatment processes such as T73, T74 and T76 have been developed recently to improve the corrosion resistance of aluminium alloys [14,

15]. Unfortunately, the alloy strength was simultaneously decreased by 5%–15% after applying these ageing processes. On the other hand, a retrogression and re-ageing (RRA) treatment was developed [16] to be able to obtain good corrosion resistance without significantly sacrificing the strength through forming fine precipitates inside the primary grains and coarse precipitates at grain boundaries [17,18]. Although the precipitates of  $\eta'$  phase have been widely studied for Al–Zn–Mg–Cu alloys [5,19,20]. However, the strengthening mechanism of metastable  $\eta'$  phase is still not fully understood in Al–Zn–Mg–Cu alloys, in particular, limited information can be found for the orientation relationships and interface structure of  $\eta'$  phase.

Therefore, in the present study, we attempted to systematically investigate the effect of various ageing treatments on mechanical properties and corrosion behaviour of an Al–Zn–Mg–Cu alloy. And, the corresponding microstructure under various ageing treatment conditions was further studied by scanning electron microscopy (SEM) and transmission electron microscopy (TEM). And, the polarisation curves were used to analyse the corrosion behaviour of experimental alloys under the various ageing treatments. Furthermore, based on the microstructures, the crystallographic interface and morphology of the  $\eta'$  precipitates under the  $[112]_{\text{Al}}$  zone axis were analysed and discussed by means of the Transform Matrix calculation and the Fourier filtering technique. Finally, a new diffraction pattern model for  $\eta'$  phase was established in the  $[112]_{\text{Al}}$  zone axis.

## 2. Experimental

The Al–6.0Zn–2.3Mg–1.8Cu–0.1Zr (wt.%) alloy was used as starting materials with a sample size of  $20 \times 20 \times 2$  mm. The samples were solution-treated at 470 °C for 1 h in a salt bath furnace, followed by immediate quenching into cold water to room temperature. Then, the samples undergone various ageing treatment conditions including T6, T74 and RRA to investigate the mechanical properties, corrosion performance and microstructure. The details of the ageing processes were listed in Table 1.

Mechanical property test was performed on smooth plate specimens by an Instron 3369 testing machine at room temperature with a tensile speed of 2 mm/min. The gauge length and width of the specimen were 25 mm and 6 mm, respectively. The intergranular corrosion test was performed according to the standard of GB7998–2005 [21]. The corrosion medium was the solution of 57 g/L NaCl + 10 mol/L H<sub>2</sub>O<sub>2</sub>, and the testing temperature was  $35 \pm 1$  °C. After 6 h immersion in the corrosion medium, the samples were cleaned and sectioned perpendicular to a corroded surface, followed by standard grinding and polishing. Then, the maximum intergranular corrosion depth was measured to evaluate the corrosion performance. Furthermore, the accelerated exfoliation corrosion test was performed at room temperature according to the EXCO test method described in ASTM G34–01 [22]. The EXCO test solution consisted of 4.0 mol/L NaCl + 0.5 mol/L KNO<sub>3</sub> + 0.1 mol/L HNO<sub>3</sub> at 0.4 pH. The electrolyte volume–electrode surface area ratio was 15 mL/cm<sup>2</sup>. After 48 h immersion in the EXCO solution, the corrosion morphologies with various ageing treatments were recorded. The slow strain rate test (SSRT) in air and in a 3.5 wt.% NaCl water solution was carried out to investigate the SCC resistance according to GB 15970.7–2000 with a strain rate of  $10^{-6}$  s<sup>-1</sup> [23].

**Table 1**

Details of the heat treatment processes used for the experimental Al–Zn–Mg–Cu alloy.

Temper	Heat treatment process
T6	470 °C/1 h + water quench + 120 °C/6 h
T74	470 °C/1 h + water quench + 120 °C/6 h + 160 °C/16 h
RRA40	470 °C/1 h + water quench + 120 °C/24 h + 180 °C/40 min + 120 °C/24 h
RRA60	470 °C/1 h + water quench + 120 °C/24 h + 180 °C/60 min + 120 °C/24 h

FEI Sirion 200 SEM was used to observe the fracture morphology. Typical specimens at various ageing treatment conditions were selected for the detailed TEM and high resolution transmission electron microscopy (HRTEM) examinations. The specimens for TEM were prepared by a standard electro-polishing procedure. The electrolytic solution was a mixture of nitric acid and methyl alcohol (1:4). The electrolytic polishing was operated at 22 V from –20 °C to –30 °C. A JEOL-2100F HRTEM was used for the microstructural investigation.

## 3. Results

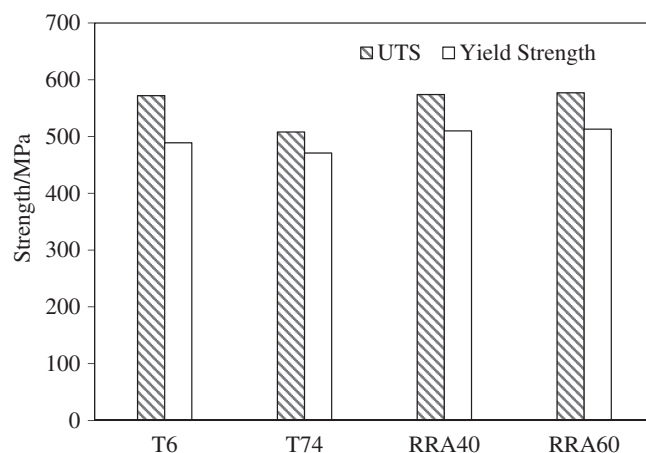
### 3.1. Effects of heat treatments on the strength

Fig. 1 presented the mechanical properties of the experimental alloy under various ageing treatment conditions. For the T6 temper sample, the ultimate tensile strength (UTS) and yield strength (YS) were 572 MPa and 489 MPa, respectively. Compared with the T6 temper, the UTS and YS of the T74 temper sample decreased 11.2% and 3.7%, respectively. The UTS and YS of the RRA40/RRA60 temper samples were 574 Mpa/577 MPa and 510 Mpa/513 MPa, respectively. Both of them were slightly higher than that of T6 temper but significantly higher than that of T74 temper. In conclusion, the strength was in the following order: RRA60 > RRA40 > T6 > T74.

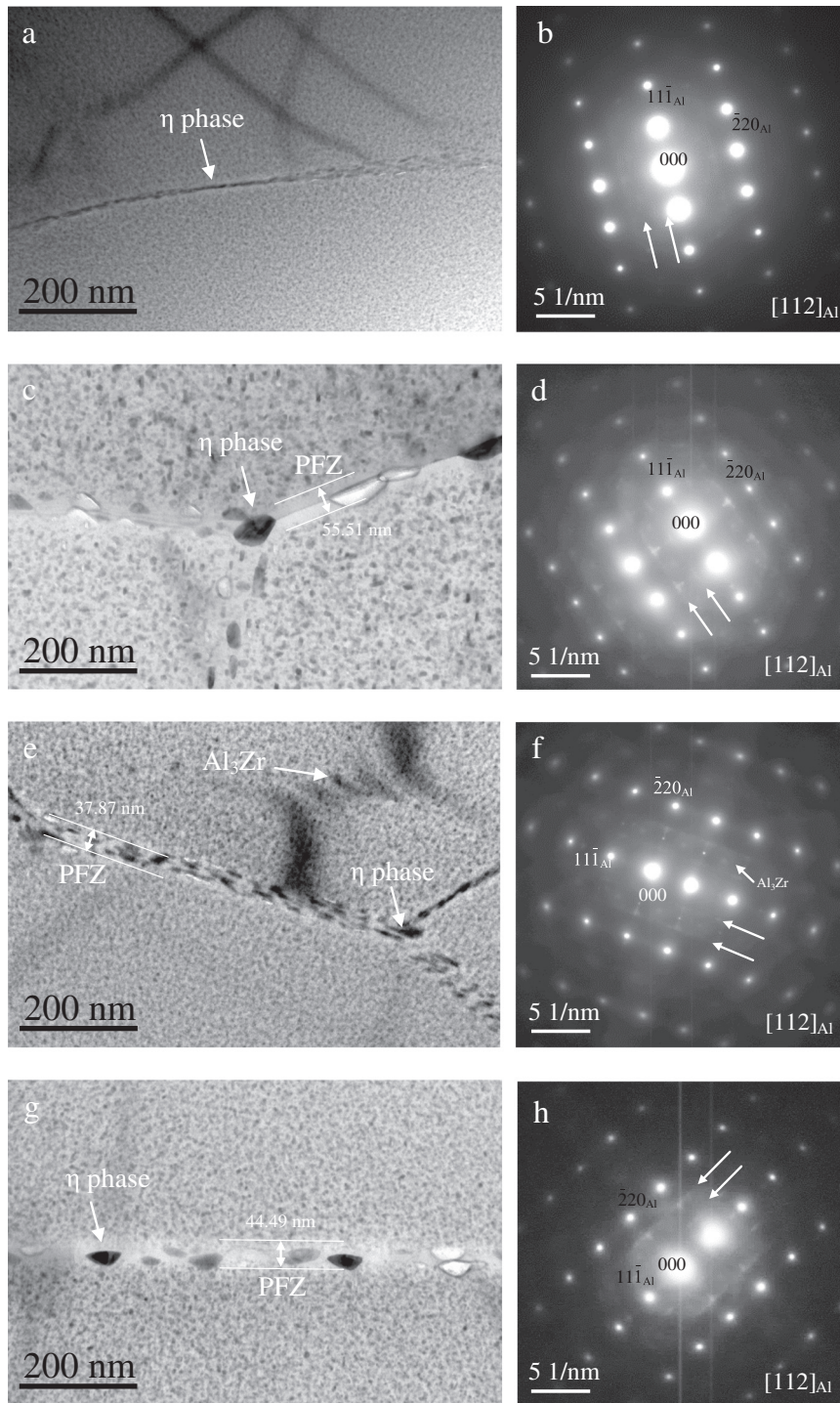
### 3.2. Microstructures with the various heat treatment conditions

Fig. 2 showed the bright-field TEM images and the corresponding selected area diffraction patterns (SADPs) of the Al–Zn–Mg–Cu alloy with different heat treatment conditions under the  $\langle 112 \rangle_{\text{Al}}$  zone axis. In the T6 sample in Fig. 2a, it was observed that a large number of fine precipitates with 2–5 nm size were homogeneously distributed in the Al matrix. The SADP was shown in Fig. 2b. Except the diffraction spots from the Al matrix, some weak diffraction streaks were also observed at the  $1/3$  and  $2/3$   $220_{\text{Al}}$  positions, which indicated that the fine  $\eta'$  phases had been precipitated [24], although they were not predominate in the microstructure. Generally, the combination of GP zones and  $\eta'$  phase resulted in the strengthening at T6 heat treatment [7]. At the same time, some precipitates were also observed at the grain boundaries with a continuous distribution. The precipitates at the grain boundaries were 4–10 nm in size, implying the formation of the equilibrium  $\eta$  phase.

Fig. 2c and d represented the TEM images and the corresponding SADP of the T74 sample. Compared with the microstructure obtained under T6 treatment, the precipitates obtained by T74 treatment were coarser with about 10–20 nm size in the matrix. However, it was obvious that the precipitates presented a discontinuous distribution along grain



**Fig. 1.** Mechanical properties of the experimental alloy various ageing treatment conditions.



**Fig. 2.** TEM images and the corresponding  $[112]_{\text{Al}}$  SADPs of the Al-Zn-Mg-Cu alloy aged under (a, b) T6, (c, d) T74, (e, f) RRA40, and (g, h) RRA60. The parallel arrows showed the diffraction streaks from the  $\eta'$  precipitates in all the SADPs.

boundaries with larger size of about 50 nm as shown by the arrow in Fig. 2c. Simultaneously, it was found that a PFZ with 55.51 nm width had been formed. In addition, the diffraction spots at  $1/3$  and  $2/3$   $220_{\text{Al}}$  positions became stronger, which indicated that these precipitates were still the  $\eta'$  phase.

The TEM images and the corresponding SADP of RRA samples were shown in Fig. 2e and f (RRA40) and Fig. 2g and h (RRA60), respectively. It was clear that the morphology of precipitates in the matrix under RRA40 and RRA60 treatments was similar. Their sizes were 5–10 nm, which were coarser than that in Fig. 2a, but were finer than that in

Fig. 2c. Meanwhile, the  $\eta$  precipitates at grain boundaries exhibited a discontinuous distribution, which was similar to that obtained in T74 ageing. In addition, it should be noted that the width (44.49 nm) of PFZ in the RRA60 sample was also obviously bigger than (37.87 nm) in the RRA40 sample. The corresponding SADP confirmed that these precipitates in the Al matrix were still  $\eta'$  phase. In all the SADPs, some weak diffraction spots near  $1/2$   $311_{\text{Al}}$  position, which was most likely from GPII zone, were observed [25,26]. In addition, the diffraction spots from the  $\text{Al}_3\text{Zr}$  phase in the  $1/2$   $220_{\text{Al}}$  position, were also observed in Fig. 2h.

### 3.3. Effect of the various heat treatment conditions on corrosion behaviours

Because Al–Zn–Mg–Cu alloys were sensitive to the localised corrosion, such as intergranular corrosion, exfoliation corrosion and SCC, and the corrosion was closely related to the microstructure, therefore, the effects of the heat treatments on the corrosion behaviours and microstructures were investigated. Fig. 3 showed the morphology of the samples after intergranular corrosion testing. It was obvious that the depth of intergranular corrosion was at the maximum value of 176  $\mu\text{m}$  under the T6 treatment in Fig. 3a, and at the minimum value of 54  $\mu\text{m}$  under the T74 treatment in Fig. 3b. The depth of intergranular corrosion was 105  $\mu\text{m}$  for the RRA40 samples and 84  $\mu\text{m}$  for the RRA60 samples (Fig. 3c and d). Clearly, the corrosion depths of the RRA samples were between that of the T6 and T74 samples. Therefore, the order of the resistance to the intergranular corrosion was T6 < RRA40 < RRA60 < T74.

Fig. 4 further presented the morphologies of the exfoliation corrosion of the Al–Zn–Mg–Cu alloy with different heat treatments. It was found that the alloys presented obvious exfoliation corrosion. The T6 samples showed the worst exfoliation corrosion (Fig. 4a), where blisters were often observed and several peeling-off areas were seen on the sample surface. In contrast, in the samples obtained from T74 to RRA treatments, the numbers of blisters on the surface were obviously decreased and much less localised peelings were observed (Fig. 4b to d). In particular, when the alloy was processed at T74 treatment, the exfoliation corrosion susceptibility was significantly improved because the numbers of blisters were much less in quantity and very fine in size. Therefore, the surface quality observations confirmed that the order of the resistance to exfoliation corrosion was T6 < RRA40 < RRA60 < T74.

Furthermore, the typical stress–displacement curves of the SCC tests for different heat treatments were shown in Fig. 5. According to the

reports in ref. [27–29], the SCC susceptibility could be evaluated by a ratio  $r_{tf}$ , which was calculated by:

$$r_{tf} = \frac{t_{fe}}{t_{fc}} \quad (1)$$

where  $t_{fe}$  was the measurement of time-to-failure determined in a 3.5 wt.% NaCl aqueous solution and  $t_{fc}$  was the corresponding value determined in air. The greater the  $r_{tf}$  values, the better the SCC-resistance becomes. In addition to the ratio  $r_{tf}$ , some researchers also adopted the strength loss to evaluate the SCC susceptibility, which was calculated by:

$$\text{Strength loss} = \frac{\sigma_{air} - \sigma_{medium}}{\sigma_{air}} \times 100\% \quad (2)$$

where  $\sigma_{air}$  was the UTS in air and  $\sigma_{medium}$  was the UTS in the 3.5 wt.% NaCl aqueous solution.

The strength loss and  $r_{tf}$  for the different conditions are listed in Table 2. According to the results in Fig. 5 and Table 2, all the SSRT specimens provided lower UTS in the 3.5 wt.% NaCl solution than that in air, but the strength loss was not significant. Therefore, the SCC susceptibility was further evaluated by the ratio  $r_{tf}$ . It was found that the samples treated in the 3.5 wt.% NaCl solution had a smaller displacement than that treated in air. In the T6 samples, the strength was decreased suddenly while fracturing, and the samples showed the lowest  $r_{tf}$  (0.7835), therefore, it had the highest SCC susceptibility. Compared with the T6 samples, the RRA samples had higher  $r_{tf}$  values of 0.7919 for RRA40 samples and 0.8755 for RRA60 samples, which indicated that RRA conditions could obviously improve the stress corrosion resistance of the Al–Zn–Mg–Cu alloy. However, the  $r_{tf}$  under the T74 condition presented the largest value (0.9130) among all of the testing samples,

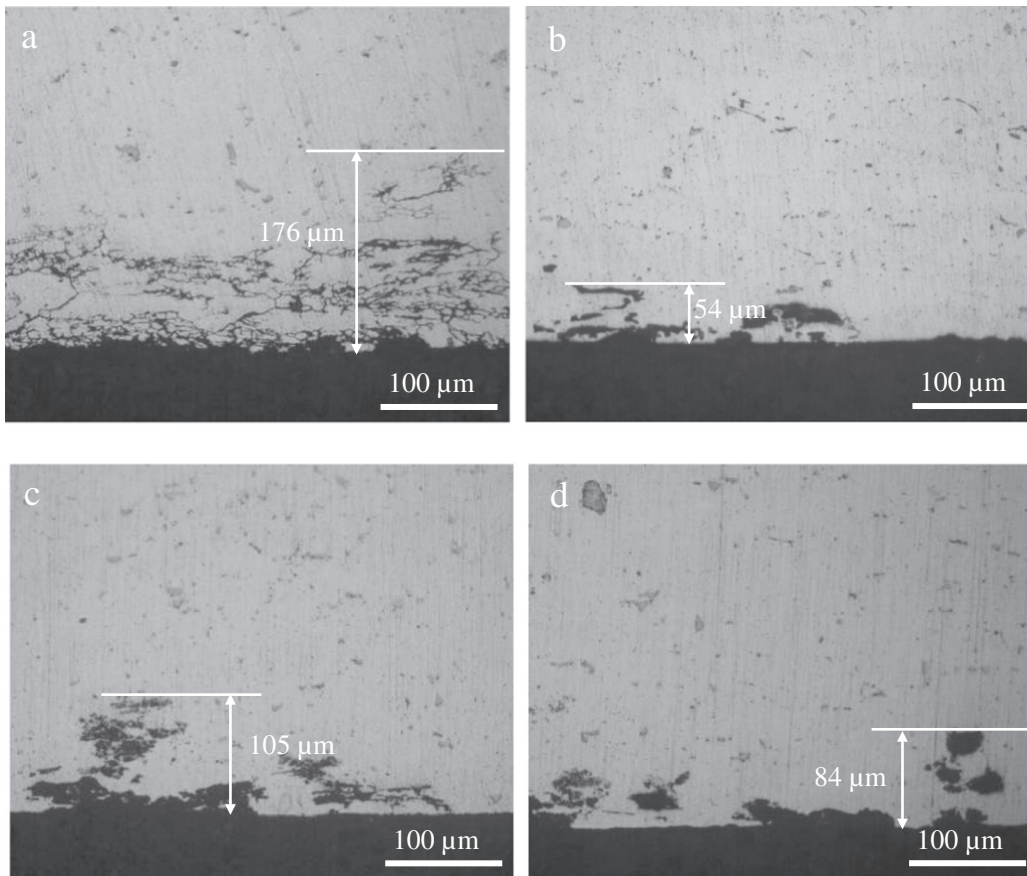
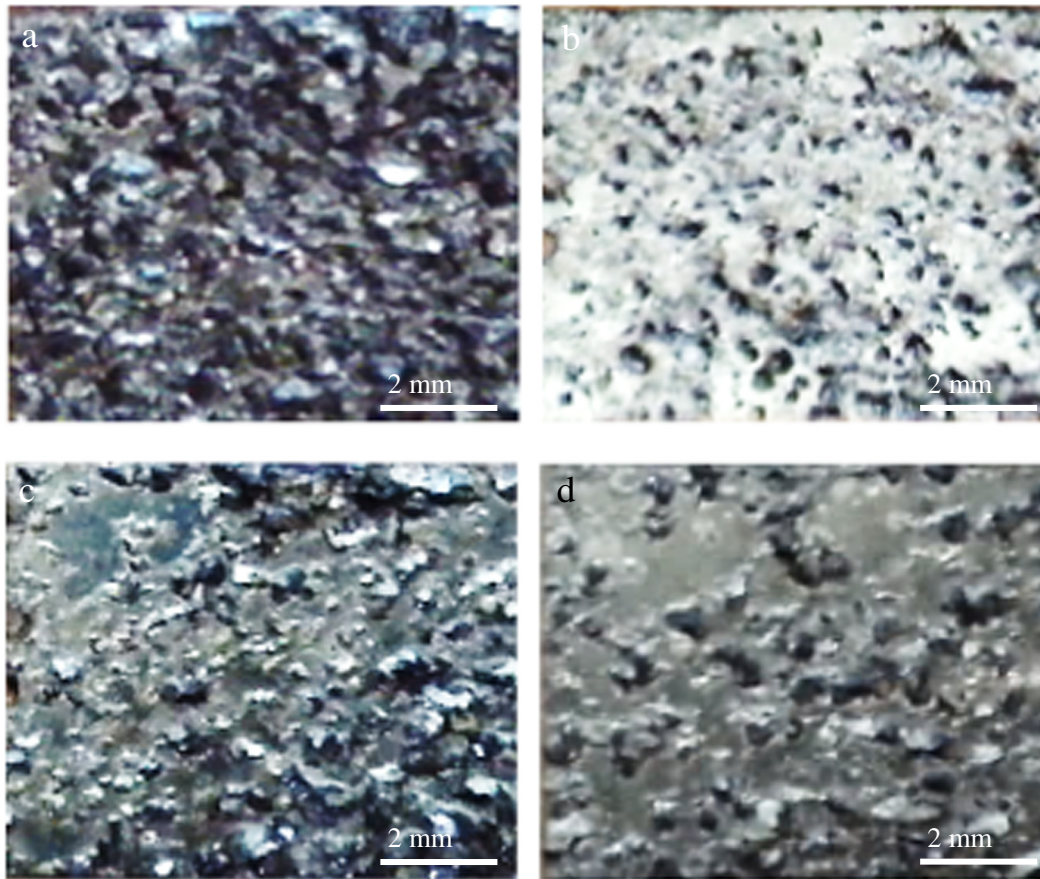


Fig. 3. The morphologies of the intergranular corrosion of the Al–Zn–Mg–Cu alloy aged under (a) T6, (b) T74, (c) RRA40, and (d) RRA60.



**Fig. 4.** The morphologies of the exfoliation corrosion of the Al-Zn-Mg-Cu alloy aged under different heat treatment conditions and immersed 48 h in the EXCO solution, (a) T6, (b) T74, (c) RRA40, and (d) RRA60.

which indicated that the T74 samples had the lowest SCC susceptibility. In addition, the RRA60 samples showed slightly different features in comparison with the T74 samples. Although the RRA60 samples had lower  $r_{if}$  values, the strengths were higher for the samples treated in air and the NaCl solution. Therefore, the RRA60 samples exhibited the best combination of the strength and SCC resistance.

Fig. 6 further presented the tensile fracture surfaces of the samples tested in the 3.5 wt.% NaCl aqueous solution. The fracture surface of the T6 sample presented numerous turtle cracks as shown in Fig. 6a, however, no any dimples could be observed. Therefore, the grains were obviously attacked along the grain boundaries, revealing the typical intergranular fracture morphology. In contrast, in the T74

sample in Fig. 6b, the numbers of cracking were obviously decreased. The fracture surface was dominated by the intergranular microvoid coalescences and transgranular morphologies. Furthermore, both the RRA samples exhibited the existence of dimples, clear tearing edges and intergranular corrosion cracking on the surface in Fig. 6c and d, resulting in the intergranular fracture. Therefore, the T6 samples had the worst SCC resistance, and the T74 samples had the best SCC resistance.

Fig. 7 showed the polarisation curves of the alloy with different heat treatments in the EXCO solution. After analysing these polarisation curves by Tafel extrapolation method, the related electrochemical parameters could be obtained and the results were shown in Table 3.

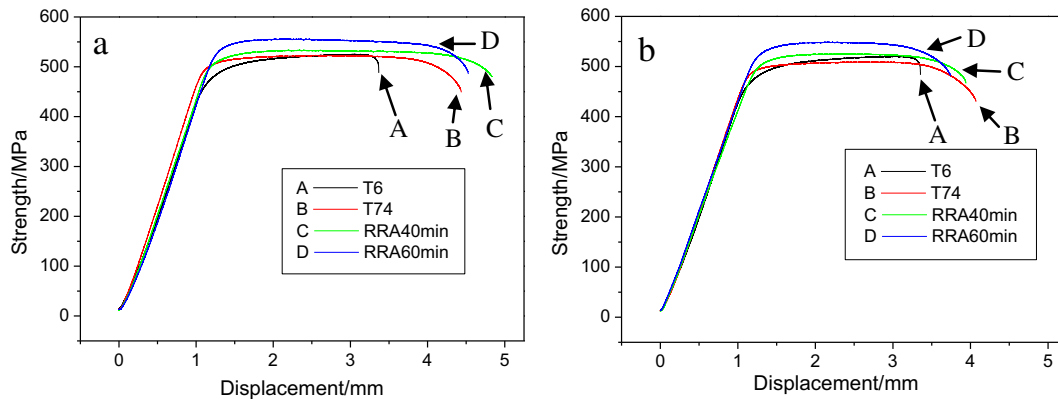


**Fig. 5.** Stress-displacement curves of the Al-Zn-Mg-Cu alloy aged under different heat treatment processes in (a) air and (b) 3.5 wt.% NaCl solution conditions.

**Table 2**  
Ultimate tensile strength and fracture time of the Al-Zn-Mg-Cu alloy with various heat treatment processes in SSRT test.

	UTS (MPa)			Time (h)		
	In air	In 3.5 wt.% NaCl	Strength loss (%)	In air	In 3.5 wt.% NaCl	$t_{fj}$
T6	524	522	0.38	31.15	24.60	0.7835
T74	512	508	0.78	41.05	37.77	0.9130
RRA40	531	529	0.38	43.88	34.75	0.7919
RRA60	551	547	0.73	41.87	36.58	0.8755

It was obvious that the heat treatments altered the electrochemical response. Generally, the more positive the corrosion potential  $E_{corr}$ , and the smaller the current  $I_{corr}$ , the better corrosion resistance the alloy presented [13]. As seen, the T6 sample had the lowest and the T74 samples had the highest corrosion potential. The RRA samples were in between of the values given by T6 and T74 samples. However, the potentials of the Al-Zn-Mg-Cu alloy were shifted with the prolonged retrogression time, indicating that the corrosion susceptibility was decreased. Therefore, as seen from Table 3, the order of corrosion resistance with various heat treatments should be described as: T6 < RRA40 < RRA60 < T74, which was also consistent with the results of the intergranular corrosion, exfoliation corrosion and SCC tests shown in Figs. 3 to 6.

#### 4. Discussion

According to the experimental results, the ageing process is dominant for the formation of  $\eta'$  precipitates in the microstructure, which are critical to provide the strengthening and improve the corrosion resistance. Generally, the alloy can be strengthened by the interaction of dislocation migration with the precipitates. A coherent or semi-coherent stress-field around a precipitate can more effectively prevent the dislocation movement. Therefore, the knowledge of the orientation relationships and the

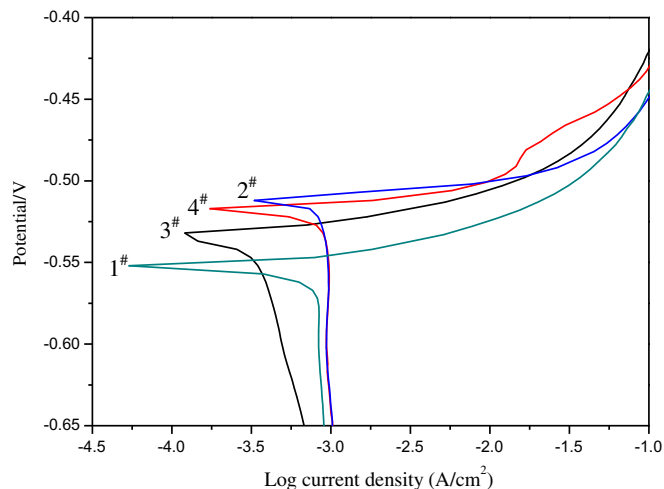


**Fig. 7.** The polarisation curves of the Al-Zn-Mg-Cu alloy aged under different processes. 1#-T6 (470 °C/1 h + 120 °C/6 h), 2#-T74 (470 °C/1 h + 120 °C/6 h + 160 °C/16 h), 3#-RRA40 (470 °C/1 h + 120 °C/24 h + 180 °C/40 min + 120 °C/24 h) 4#-RRA60 (470 °C/1 h + 120 °C/24 h + 180 °C/60 min + 120 °C/24 h).

interface characteristics of the precipitates with the Al matrix are essential for understanding the strength enhancement.

##### 4.1. Diffraction analysis and orientation relationships of $\eta'$ phase

Previous researches had confirmed that the  $\eta'$  phases actually have four variants along four different  $\{111\}_{Al}$  planes [20,30]. Therefore, the SADP from the  $\eta'$  phases in Fig. 2 should actually be complex mixing electron diffraction patterns. Fig. 8a presented a HRTEM image from one  $\eta'$  variant under the  $[112]_{Al}$  zone axis, where its long axis was along the  $(1\bar{1}1)_{Al}$  plane. The corresponding fast Fourier transform

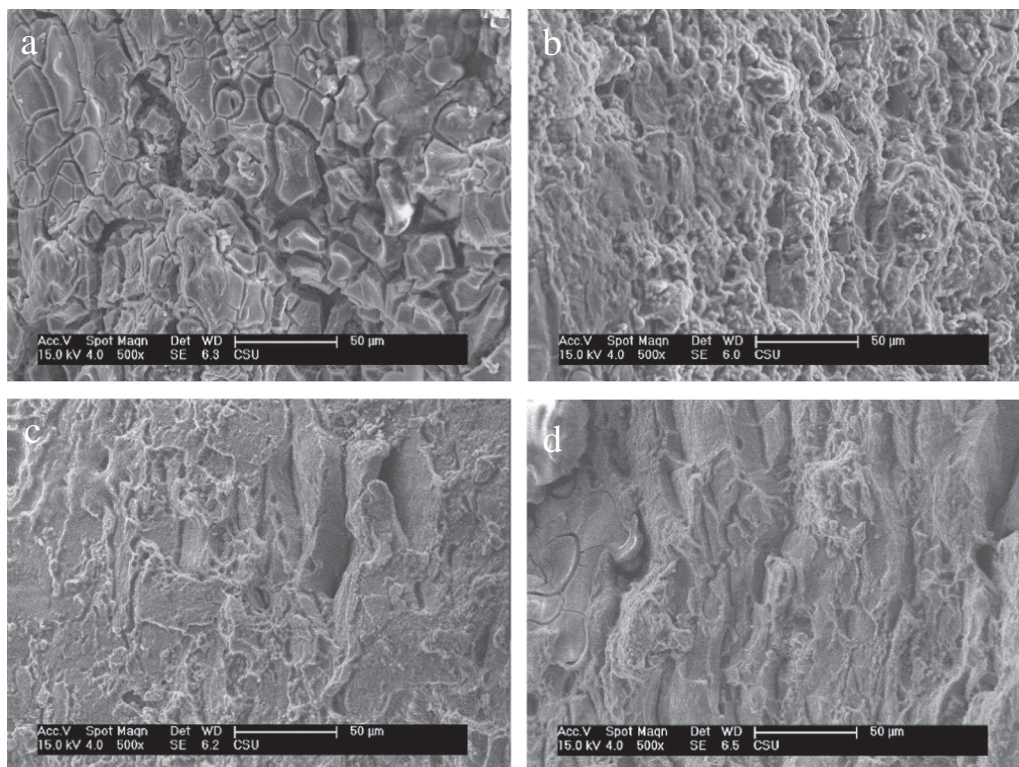


**Fig. 6.** The morphologies of the SCC tensile fracture of the Al-Zn-Mg-Cu alloy under different heat treatment conditions in the 3.5% NaCl solution, (a) T6, (b) T74, (c) RRA40, and (d) RRA60.

**Table 3**

The corrosion parameters of polarisation curves of the Al–Zn–Mg–Cu alloy with various heat treatment processes.

Heat treatment	$E_{corr}$ (V)	$I_{corr}$ ( $\text{mA} \cdot \text{cm}^{-2}$ )	$R_p$ ( $\Omega \cdot \text{cm}^{-2}$ )
T6	−0.572	1.494	25.3
T74	−0.511	0.380	41.1
RRA40	−0.542	0.539	31.3
RRA60	−0.515	0.512	37.7

(FFT) was displayed in Fig. 8b, where clear diffraction streaks were located at the  $1/3$  and  $2/3$   $220_{\text{Al}}$  positions from the  $\eta'$  phase.

The orientation relationships could be confirmed by the Transition Matrix calculation. According to our previous research [20], Transition Matrix  $M(d)$  and  $M(p)$  between two directions and two planes were summarised in Table 4.  $M(p)$  was the inverse of Transpose Matrix of  $M(d)$ . Therefore, all of the orientation relationships of four  $\eta'$  variant could be transformed in the given  $[112]_{\text{Al}}$  zone axis, as shown in Table 4. By calculation, it was noted that when four  $\eta'$  variants were precipitated under the  $[112]_{\text{Al}}$  zone axis, only variant 1 and variant 3 present any specific orientation relationships, but variant 2 and variant 4 do not present any orientation relationships with the Al matrix. Therefore, the  $\eta'$  phases actually had only two zone axes:  $[\bar{1}2\bar{1}3]_{\eta'}$  and  $[108\bar{2}3]_{\eta'}$ , parallel to the  $[112]_{\text{Al}}$  zone axis when they were precipitated from the Al matrix. Furthermore, the simulated diffraction patterns of two  $\eta'$

variants under different zone axes were displayed in Fig. 9, which was observed along the  $[112]_{\text{Al}}$  direction of Al matrix. Fig. 9a and b displayed the diffraction patterns under the  $[\bar{1}2\bar{1}3]_{\eta'}$  and  $[108\bar{2}3]_{\eta'}$  zone axes from variant 1 to variant 3, respectively. By overlapping the two simulated diffraction patterns of  $\eta'$  phases with the  $[112]_{\text{Al}}$  diffraction patterns of the Al matrix, a model of mixing SADP under the given  $[112]_{\text{Al}}$  zone axis had been obtained and the results were shown in Fig. 9c. The black, blue and red diffraction spots were from the Al matrix, variant 1 and variant 3, respectively. It should be noted that the atom coordinates and structure factors of the  $\eta'$  phase with chemical formula  $\text{Mg}_4\text{Zn}_{13}\text{Al}_2$  had been considered during the simulation process based on the Model II and the composition proposed by Kverneland [30]. It was obvious that the diffraction pattern model in Fig. 9c was basically consistent with the experimental results in Fig. 2, where the diffraction streaks located at the  $1/3$  and  $2/3$   $220_{\text{Al}}$  positions could be explained by this model. Furthermore, based on the calculation results in Table 3, the orientation relationships between the  $\eta'$  precipitates and the Al matrix under the  $[112]_{\text{Al}}$  zone axis could be described as:  $[\bar{1}2\bar{1}3]_{\eta'}/[112]_{\text{Al}}; (1\bar{2}12)_{\eta'}/(11\bar{1})_{\text{Al}}$  and  $[108\bar{2}3]_{\eta'}/[112]_{\text{Al}}; (11\bar{2}2)_{\eta'}/(11\bar{1})_{\text{Al}}$ .

#### 4.2. Crystallographic interface and the morphology of $\eta'$ phase

Based on the orientation relationships obtained above, the interface between the  $\eta'$  phase and the Al matrix could be analysed by the crystallography and the Fourier filtering technique. As seen from

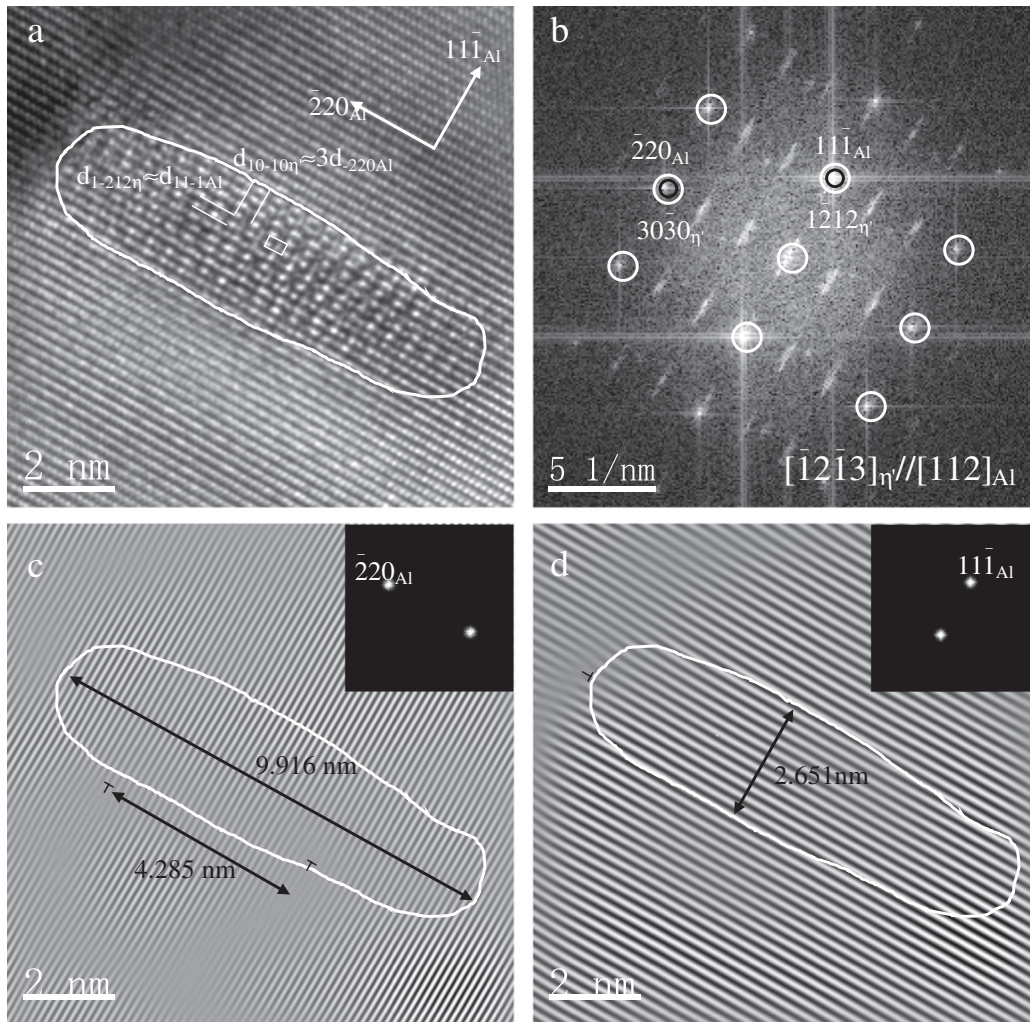


**Fig. 8.** The crystallographic interface and the morphology of the  $\eta'$  phase under the  $[112]_{\text{Al}}$  zone axis. (a) HRTEM image, (b) the corresponding FFT pattern, (c) IFFT image of selected  $220_{\text{Al}}$  and  $3030_{\eta'}$  reflections and (d) IFFT image of selected  $11\bar{1}_{\text{Al}}$  and  $1212_{\eta'}$  reflections. The interface dislocations were marked by black symbols.

**Table 4**

Transition Matrix  $M(d)$  and  $M(p)$  of four variants of  $\eta'$  precipitates [20], and the corresponding orientation relationships based on the Transition Matrix calculation under the given  $[112]_{Al}$  zone axis.

Variants	$M(d)$	$M(p)$	The corresponding orientation relationships under the given $[112]_{Al}$ zone axis				
1	$-2/3$	$2/3$	0	$-1/2$	1	$-1/2$	$[\bar{1}2\bar{1}3]_{\eta'}/[112]_{Al};(\bar{1}212)_{\eta'}/(11)_{Al}$
	$-2/3$	0	$2/3$	$-1/2$	$-1/2$	1	
	$1/6$	$1/6$	$1/6$	2	2	2	
2	$2/3$	$2/3$	0	1	$1/2$	$1/2$	-
	$-2/3$	$2/3$	0	$-1$	$1/2$	$-1/2$	
	0	$2/3$	$2/3$	$1/2$	$1/2$	1	
3	$2/3$	$2/3$	0	1	$1/2$	$1/2$	$[10\bar{8}23]_{\eta'}/[112]_{Al};(1\bar{1}22)_{\eta'}/(1\bar{1}\bar{1})_{Al}$
	0	$2/3$	$-2/3$	$-1/2$	$1/2$	$-1$	
	$-1/6$	$1/6$	$1/6$	$-2$	2	2	
4	$1/6$	$1/6$	$-1/6$	2	2	$-2$	-
	0	$2/3$	$2/3$	$-1/2$	$1/2$	1	
	$1/6$	$-1/6$	$1/6$	2	$-2$	2	

Fig. 8a, the  $\eta'$  phase presented obvious periodic lattice fringes in the HRTEM image, where the white-rectangle depicted a projection image of one unit cell of  $\eta'$  phase along the  $[\bar{1}2\bar{1}3]_{\eta'}$  direction. According to the model described in Fig. 9c, there was a near coincidence between  $30\bar{3}0_{\eta'}$  and  $\bar{2}20_{Al}$  reflections, and  $10\bar{2}12_{\eta'}$  and  $1\bar{1}\bar{1}_{Al}$  reflections, respectively. Therefore, the interfaces between the two phases could be further studied in detail. Selecting the two sets of parallel planes and applying the Fourier filter technology, two inverse Fourier filter transformation (IFFT) images could be seen in Fig. 8c and d, respectively. It was obvious that the interface dislocations between the  $\eta'$  phase and the Al matrix could be observed (marked by the white symbols).

For the  $\eta'$  precipitate with a HCP structure, the spacing  $d$  could be calculated by the equation:

$$\frac{1}{d^2} = \frac{4}{3a^2} (h^2 + hk + k^2) + \frac{l^2}{c^2} \quad (3)$$

where  $a$  and  $c$  were the lattice parameters of HCP structure. And,  $h$ ,  $k$  and  $l$  were the plane indices. As seen from Fig. 8c and d, the measured distance along the  $[220]_{Al}$  and  $[1\bar{1}\bar{1}]_{Al}$  directions was 9.916 nm and 2.651 nm, respectively. The corresponding numbers of crystal planes were 67 and 11, respectively. Therefore, according to the obtained orientation relationships and the FFT patterns, the calculated spacing of  $(30\bar{3}0)_{\eta'}$  plane and  $(\bar{1}212)_{\eta'}$  plane was 0.418 nm and 0.241 nm, respectively. The lattice parameters of the  $\eta'$  precipitate could be further deduced from Eq. (3) as:  $a = 0.513$  nm and  $c = 1.409$  nm, which were basically consistent with the lattice parameters  $a = 0.496$  nm and  $c = 1.402$  nm, proposed by Kverneland [30].

In addition, two interface dislocations along the  $[220]_{Al}$  direction in Fig. 8c were also found. Therefore, based on the lattice parameters obtained for the  $\eta'$  precipitate ( $a = 0.513$  nm and  $c = 1.409$  nm), the lattice misfit  $\delta$  between the  $\eta'$  precipitate and the Al matrix could be calculated as only 3.4% by:

$$\delta = \frac{2(d_1 - d_2)}{d_1 + d_2} \quad (4)$$

where  $d_1$  and  $d_2$  were the spacing of two parallel crystal planes, respectively. Furthermore, the distance  $D$  between the interface dislocations could be obtained as 4.250 nm by:

$$D = \frac{(d_1 + d_2)^2}{4(d_1 - d_2)} \quad (5)$$

Obviously, the calculated distance was in good agreement with the experimental value, which was 4.285 nm in Fig. 8c.

Overall, the 4.3% misfit indicated that the  $\eta'$  precipitates exhibited semi-coherent interfaces with the Al matrix under the  $[112]_{Al}$  zone axis, which inevitably introduced a semi-coherent strain field between the individual  $\eta'$  precipitate and the adjacent Al matrix. Consequently, the  $\eta'$  precipitates became the effective obstacles of dislocation movement to strengthen the alloy.

#### 4.3. Relationships between the microstructure and the properties

As seen in Fig. 2, the  $\eta'$  precipitates formed at various ageing treatment conditions played an important role in controlling the strength of

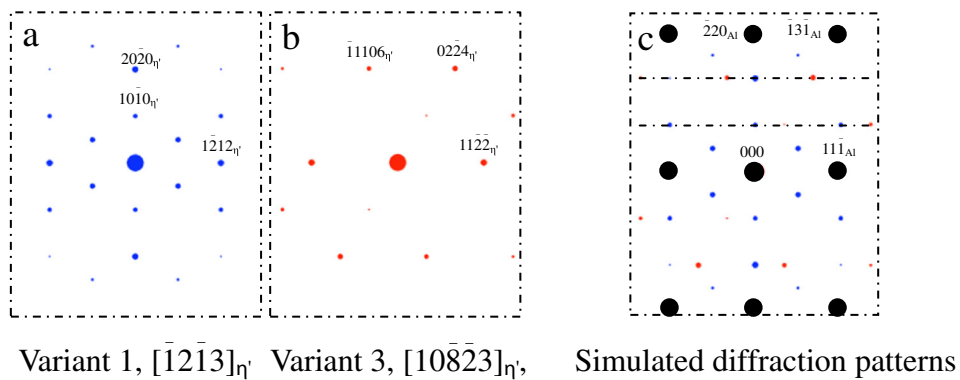


**Fig. 9.** Diffraction pattern analysis of the  $\eta'$  phase under the  $[112]_{Al}$  zone axis, (a) calculated diffraction patterns from  $\eta'$  variant 1 under the given  $[112]_{Al}$  zone axis, (b) calculated diffraction patterns from  $\eta'$  variant 3 under the given  $[112]_{Al}$  zone axis, and (c) the overlapped diffraction patterns of two  $\eta'$  variants and Al matrix under the  $[112]_{Al}$  zone axis. The black, blue and red diffraction spots were from Al matrix, variant 1 and variant 3, respectively, and the dashed lines represented the characteristic diffraction streaks from the  $\eta'$  precipitates in (c). (For interpretation of the references to color in this figure legend, the reader is referred to the web version of this article.)

the experimental alloy. In the samples processed by T6, the  $\eta'$  precipitates in Al grains were fine and distribute homogeneously with only 2–5 nm in size and with a high number density. In the samples with the over-aged T74 process, the sizes of the  $\eta'$  precipitate were increased to 10–20 nm, but its number density was decreased significantly. In the samples processed by RRA treatment, the size of  $\eta'$  precipitates was between 5 nm and 10 nm, which was slightly larger than that obtained in T6 process but smaller than that obtained in T74 process. And, the number density of  $\eta'$  precipitates was also higher than that obtained in T74 but lower than that obtained in T6. Based on the HRTEM observation and the interface analysis in Section 4.2, the  $\eta'$  precipitates had a semi-coherent strain field with the Al matrix under the  $[112]_{\text{Al}}$  zone axis. Therefore, the  $\eta'$  precipitates with a high number density and finer sizes could improve the strength of the Al–Zn–Mg–Cu alloy. This result could be achieved by RRA process.

The size and distribution of the  $\eta$  precipitates at grain boundaries resulted in the different corrosion properties at different heat treatments. The corrosion potentials of  $\eta$  phases, PFZ and the Al matrix were investigated as  $-0.869$  V,  $-0.57$  V and  $-0.68$  V, respectively [31]. Because the corrosion potential of  $\eta$  phases at the grain boundary was lower than that of the Al matrix, the  $\eta$  phases were the positive pole during corrosion. As seen in Fig. 2a, the  $\eta$  precipitates were distributed continuously at the grain boundaries with T6 treatment; therefore, the active corrosion paths for galvanic reaction were between the anodic  $\eta$  precipitates at the grain boundaries and the Al matrix. This resulted in the susceptibility to intergranular corrosion. However, when the alloy was processed with T74 and RRA treatments, the  $\eta$  precipitates at the grain boundaries were distributed discontinuously in Fig. 2c to h. Although the  $\eta$  precipitates still reacted with the Al matrix with different electrode potentials, the corrosion path was blocked by the discontinuous precipitates to prevent any further reaction along the grain boundaries. Therefore, the intergranular corrosion was significantly decreased. The larger spacing between the  $\eta$  precipitates along the grain boundaries would be able to provide increased capability to prevent intergranular corrosion, resulting in the much improved corrosion resistance. Furthermore, the exfoliation corrosion was developed from the intergranular corrosion because the corrosion products were accumulated at the grain boundaries during intergranular corrosion, which could emerge as a wedging force to lift the alloy surface. The more sensitive the alloy was to the intergranular corrosion, the more susceptible it was to the exfoliation corrosion. Therefore, T74 and RRA treatments could decrease the exfoliation corrosion susceptibility of the Al–Zn–Mg–Cu alloy. In addition, the RRA60 sample exhibited a better corrosion resistance than the RRA 40 sample, which could be attributed to the coarser  $\eta$  precipitates along the grain boundaries, as shown in Fig. 2e and g, although the wider PFZ was also beneficial to improve the corrosion behaviour [10,11].

Because the  $\eta$  precipitates at the grain boundaries had the different electrode potentials from the Al matrix, the anodic dissolution and critical defects were formed in the initial stage of SCC process in aqueous chloride solutions. Under the T6 condition, the  $\eta$  precipitates at the grain boundaries were continuously distributed to form corrosion channels, reduced the number of trapped hydrogen atoms, and increased the hydrogen atom diffusion at the grain boundaries. The increased hydrogen would be accumulated at the crack tip and led to hydrogen embrittlement along the grain boundaries. Consequently, T6 samples were prone to form cracking in the alloy. In contrast, the precipitates were discontinuously distributed at the grain boundaries in the alloy obtained under the T74 and RRA conditions so that the anodic reaction rate was significantly decreased. Therefore, the T6 samples had high possibility to form cracks than that of the T74 and RRA samples in SCC test.

## 5. Conclusions

The mechanical and corrosion properties of the Al–Zn–Mg–Cu alloy were investigated under various ageing treatment conditions. And the

crystallographic interface between the  $\eta'$  precipitate and the Al matrix was analysed and discussed by means of the Transform Matrix calculation and Fourier filtering technique. The main results were summarised as follows:

- (1) The RRA process could provide a good balance between the improved mechanical properties and the better corrosion resistance. The optimised RRA ageing process was  $120\text{ }^{\circ}\text{C}/24\text{ h} + 180\text{ }^{\circ}\text{C}/60\text{ min} + 120\text{ }^{\circ}\text{C}/24\text{ h}$  for the experimental Al–Zn–Mg–Cu alloy.
- (2) The ageing process could significantly affect the corrosion resistance. The sequence of intergranular corrosion, exfoliation corrosion and stress corrosion was in an order of  $T74 < RRA60 < RRA40 < T6$ . The improved corrosion resistance resulted from the discontinuously distributed fine  $\eta$  precipitates at the grain boundaries.
- (3) The  $\eta'$  precipitates were vital for strengthening effect. The HRTEM interface analysis revealed the existence of a semi-coherent stress field between the  $\eta'$  precipitates and the Al matrix. Transition Matrix calculation showed that the  $\eta'$  phases had only two zone axes:  $[T2T3]_{\eta'}$  and  $[10823]_{\eta'}$ , parallel to the  $[112]_{\text{Al}}$  zone axis when they were precipitated from the Al matrix. The orientation relationships with Al matrix under the  $[112]_{\text{Al}}$  zone axis could be described as:  $[T2T3]_{\eta'}/[112]_{\text{Al}}$ ;  $(T212)_{\eta'}/(1TT)_{\text{Al}}$  and  $[10823]_{\eta'}/[112]_{\text{Al}}$ ;  $(1T22)_{\eta'}/(1TT)_{\text{Al}}$ . Furthermore, the established diffraction pattern model from the  $\eta'$  precipitates in two variants under the  $[112]_{\text{Al}}$  zone axis showed a good agreement with the experimental data.

## References

- [1] W.S. Miller, L. Zhuang, J. Bottema, A.J. Wittebrood, P. De Smet, A. Hasler, A. Vieregge, Recent development in aluminum alloys for the automotive industry, *Mater. Sci. Eng. A* 50 (2000) 37–49.
- [2] A. Heinz, A. Haszler, C. Keidel, S. Moldenhauer, R. Bendictus, W.S. Miller, Recent development in aluminium alloys for aerospace applications, *Mater. Sci. Eng. A* 280 (2000) 102–107.
- [3] T. Dursun, C. Soutis, Recent developments in advanced aircraft aluminium alloys, *Mater. Des.* 56 (2014) 862–871.
- [4] S.K. Panigrahi, R. Jayaganthan, Development of ultrafine grained high strength age hardenable Al 7075 alloy by cryorolling, *Mater. Des.* 32 (2011) 3150–3160.
- [5] G. Sha, A. Cerezo, Early-stage precipitation in Al–Zn–Mg–Cu alloy (7050), *Acta Mater.* 52 (2004) 4503–4516.
- [6] X. Fang, Y. Du, M. Song, K. Li, C. Jiang, Effects of Cu content on the precipitation process of Al–Zn–Mg alloys, *J. Mater. Sci.* 47 (2012) 8174–8187.
- [7] J. Buha, R.N. Lumley, A.G. Crosky, Secondary ageing in an aluminium alloy 7050, *Mater. Sci. Eng. A* 492 (2008) 1–10.
- [8] J. Chen, L. Zhen, S. Yang, W. Shao, S. Dai, Investigation of precipitation behaviour and related hardening in AA 7055 aluminium alloy, *Mater. Sci. Eng. A* 500 (2009) 34–42.
- [9] Y.C. Lin, Y.Q. Jiang, X.C. Zhang, J. Deng, X.M. Chen, Effect of creep-ageing processing on corrosion resistance of an Al–Zn–Mg–Cu alloy, *Mater. Des.* 61 (2014) 228–238.
- [10] C. Li, Q. Pan, Y. Shi, Y. Wang, B. Li, Influence of aging temperature on corrosion behaviour of Al–Zn–Mg–Sc–Zr alloy, *Mater. Des.* 55 (2014) 551–559.
- [11] X.Y. Sun, B. Zhang, H.Q. Lin, Y. Zhou, L. Sun, J.Q. Wang, E.H. Han, W. Ke, Correlations between stress corrosion cracking susceptibility and grain boundary microstructures for an Al–Zn–Mg alloy, *Corros. Sci.* 77 (2013) 103–112.
- [12] C. Luo, X. Zhou, G.E. Thompson, A.E. Hughes, Observations of intergranular corrosion in AA2024–T351: the influence of grain stored energy, *Corros. Sci.* 61 (2012) 35–44.
- [13] S. Chen, K. Chen, G. Peng, L. Jia, P. Dong, Effect of heat treatment on strength, exfoliation corrosion and electrochemical behaviour of 7085 aluminium alloy, *Mater. Des.* 35 (2012) 93–98.
- [14] J.R. Davis, *Corrosion of Aluminium and Aluminium Alloys*, American Society for Metals, Materials Park, OH, 1999.
- [15] J. Thompson, E.S. Tonkins, V.S. Agarwala, A heat treatment for reducing corrosion and stress corrosion cracking susceptibilities in 7XXX aluminium alloys, *Mater. Perform.* 26 (1987) 45–52.
- [16] B. Cina, Reducing the susceptibility of alloys particularly aluminium alloys to stress corrosion cracking, US Patent, 1974.
- [17] Y. Xiao, Q. Pan, W. Li, X. Liu, Y. He, Influence of retrogression and re-ageing treatment on corrosion behaviour of an Al–Zn–Mg–Cu alloy, *Mater. Des.* 32 (2011) 2149–2156.
- [18] Y. Wang, Q. Pan, L. Wei, B. Li, Y. Wang, Effect of retrogression and reaging treatment on the microstructure and fatigue crack growth behaviour of 7050 aluminium alloy thick plate, *Mater. Des.* 55 (2014) 857–863.
- [19] J.H. Auld, S.M. Cousland, The transition phase  $\eta'$  in Al–Zn–Mg alloys, *Scr. Mater.* 5 (1971) 765–770.

- [20] W. Yang, S. Ji, M. Wang, Z. Li, Precipitation behaviour of Al-Zn-Mg-Cu alloy and diffraction analysis from  $\eta'$  precipitates in four variants, *J. Alloys Compd.* 610 (2014) 623–629.
- [21] GB7998-2005, National standard of China. Test method for intergranular corrosion of aluminium alloy.
- [22] ASTM G34-01. Standard test method for exfoliation corrosion susceptibility in 2XXX and 7XXX series aluminium alloys (EXCO test).
- [23] GB 15970.7-2000. National standard of China. Corrosion of metals and alloys-stress corrosion testing-slow strain rate testing.
- [24] X.Z. Li, V. Hansen, J. Gjønnnes, L.R. Wallenberg, HREM study and structure modelling of the  $\eta'$  phase, the hardening precipitates in commercial Al-Zn-Mg alloys, *Acta Mater.* 47 (1999) 2651–2659.
- [25] K. Stiller, P.J. Warren, V. Hansen, J. Angenete, J. Gjønnnes, Investigation of precipitation in an Al-Zn-Mg alloy after two-step ageing treatment at 100 °C and 150 °C, *Mater. Sci. Eng. A* 270 (1999) 55–63.
- [26] L.K. Berg, J. Gjønnnes, V. Hansen, X.Z. Li, M. Knutson-wedel, G. Waterloo, D. Schryvers, L.R. Wallenberg, GP-zones in Al-Zn-Mg alloys and their role in artificial aging, *Acta Mater.* 49 (2001) 3443–3451.
- [27] J.C. Lin, H.L. Liao, W.D. Jehng, C.H. Chang, S.L. Lee, Effect of heat treatments on the tensile strength and SCC-resistance of AA7050 in an alkaline saline solution, *Corros. Sci.* 48 (2006) 3139–3156.
- [28] S.A. McCluney, S.N. Popova, B.N. Popov, R.E. White, R.B. Griffin, Comparing electrochemical impedance spectroscopy methods for estimating the degree of delamination of organic coatings on steel, *J. Electrochem. Soc.* 139 (1992) 1556–1560.
- [29] D. Wang, Z.Y. Ma, Effect of pre-strain on microstructure and stress corrosion cracking of over-aged 7050 aluminium alloy, *J. Alloys Compd.* 469 (2009) 445–450.
- [30] A. Kverneland, V. Hansen, R. Vincent, K. Gjønnnes, Structure analysis of embedded nano-sized particles by precession electron diffraction  $\eta'$ -precipitate in an Al-Zn-Mg alloy as example, *Ultramicroscopy* 106 (2006) 492–502.
- [31] Z.T. Wang, R.Z. Tian, *Handbook of Aluminium Alloy and its Working*, Central South University Press, Changsha, 2000.